



저작자표시-비영리-변경금지 2.0 대한민국

이용자는 아래의 조건을 따르는 경우에 한하여 자유롭게

- 이 저작물을 복제, 배포, 전송, 전시, 공연 및 방송할 수 있습니다.

다음과 같은 조건을 따라야 합니다:



저작자표시. 귀하는 원저작자를 표시하여야 합니다.



비영리. 귀하는 이 저작물을 영리 목적으로 이용할 수 없습니다.



변경금지. 귀하는 이 저작물을 개작, 변형 또는 가공할 수 없습니다.

- 귀하는, 이 저작물의 재이용이나 배포의 경우, 이 저작물에 적용된 이용허락조건을 명확하게 나타내어야 합니다.
- 저작권자로부터 별도의 허가를 받으면 이러한 조건들은 적용되지 않습니다.

저작권법에 따른 이용자의 권리는 위의 내용에 의하여 영향을 받지 않습니다.

이것은 [이용허락규약\(Legal Code\)](#)을 이해하기 쉽게 요약한 것입니다.

[Disclaimer](#)

理學碩士學位論文

Shape-Controlled Palladium Sulfide
Nanoparticles with Desired Sulfur
Distributions for Ethanol Electrooxidation
Reaction

(에탄올 전기산화 반응에 대한 원하는 황 분포와
모양 제어된 팔라듐 황화물 나노 입자)

蔚山大學校大學院

化學科

沈馨輔

Shape-Controlled Palladium Sulfide
Nanoparticles with Desired Sulfur
Distributions for Ethanol Electrooxidation
Reaction

指導教授 홍종욱

이 論文을 理學碩士學位 論文으로 제출함

2020年 02月

蔚山大學校大學院

化學科

沈馨輔

沈 馨 輔의 理學碩士 學位 論文을 認准함

審査委員 이 민 형



審査委員 홍 종 욱



審査委員 정 재 훈



蔚 山 大 學 校 大 學 院

2020年 02月

국문요약

고분자 전해질 연료전지 PEMFC (Polymer electrolyte membrane fuel cell)는 수소와 산소가 가지고 있는 화학적 에너지를 전기 에너지로 변환시키는 에너지 변환 장치이다. 일반적으로 사용되는 전해질의 종류에 의해 구분되는 여러 형태의 연료전지 중 PEMFC는 작동 온도가 100 °C 이하로 낮고 출력 밀도가 높으며 출력 범위가 넓어 휴대용 전자 기기의 전원 장치부터 수송용 및 발전용에 이르기까지 응용분야가 다양한 특징을 가지고 있다.

PEMFC의 전극 반응은 크게 수소가 산화되는 양극(anode)과 산소가 환원되어 물이 발생하는 음극(cathode) 반응으로 구분된다. 양극의 경우, 일산화탄소 및 황의 피독에 의한 양극 촉매의 활성 저하를 막을 수 있는 내피독성 촉매의 개발이 필수적이다.

PEMFC를 구성하는 여러 핵심소재 중, 전기화학 반응이 일어나는 전극의 경우 고가의 백금 촉매가 사용되기 때문에 이로 인한 시스템 제작 비용의 상승이 상업화의 주요 걸림돌 중 하나로 인식되고 있다. 따라서 이 문제를 해결하기 위해서 백금보다 저가이면서 비슷한 촉매 활성을 나타내는 팔라듐이 대체재로 여겨지고 있다. 그 뿐만 아니라 팔라듐은 수소에 대한 강한 흡착력을 가지고 있어 수소 저장매체로도 이용되며, 센서, 정화의 역할에도 사용된다.

금속 황화물 나노 구조를 원하는 형태로 합성함으로써 다양한 전기화학적 반응에 대한 흥미로운 특성을 나타낼 수 있다. 표면 금속과 황 원자가 반응성 분자와 촉매 표면 사이의 상호 작용에 직접 영향을 미칠 수 있다. 우수한 전기 촉매 성능을 갖는 새로운 촉매를 개발하기 위해서 금속 황화물 나노 입자에서 황과 금속의 원자 분포를 조정하는 효과적인 전략이 있다. 금속 황화물 나노 구조에서 금속과 황의 원자비를 제어하기 위한 다양한 방법 중, 황화 정도의 조절 뿐만 아니라 특정 결정면으로 합성함으로써 독특한 표면 형태를 나타내어 촉매 특성에 영향을 미친다.

지금까지 팔라듐 황화물은 산화 반응에서 거의 연구되지 않았다. 실제로 팔라듐 황화물은 포면제어의 어려움으로 인해 산화반응에 활성이 높은 {100}

결정면을 가지는 나노큐브와 같은 촉매합성이 어려웠고, 따라서 팔라듐 황화물의 산화반응 활성이 높지 않은 것으로 알려져 왔다. 하지만 연구를 통해서 표면에 부분적으로 황화가 되면 활성이 향상될 수 있음을 확인하였다. 이는 부분적인 황화물로 인해서 팔라듐의 electronic structure의 변화가 있기 때문이다.

흥미롭게도 Pd_{cube}/Pd-S/I 을 제외한 황이 더 도핑된 팔라듐 황화물 나노큐브와 팔라듐 나노 큐브를 비교해봤을 때, 오히려 팔라듐 나노 큐브가 더 높은 활성을 나타내는 것을 확인할 수 있다. 이는 확실히 황의 함량이 팔라듐의 에탄올 산화 활성에 매우 밀접한 관련이 있다는 것을 보여준다. 이는 이전에 나노 입자 전체에 chalcogenide가 도핑된 metal chalcogenide (sulfide) 촉매가 물 분해 반응에서 좋은 촉매 활성을 나타낸 것과 다르게 팔라듐 황화물의 경우에는 표면의 부분적인 도핑이 촉매 활성 증진에 긍정적인 결과를 일으킨다는 것을 보여준다.

Abstract

PEMFC (polymer electrolyte membrane fuel cell) is an energy conversion device that converts the chemical energy of hydrogen and oxygen into electrical energy. Among various types of fuel cells classified by the type of electrolytes generally used, PEMFC has various characteristics due to its low operating temperature of less than 100 ° C, high power density, and wide power range. It is used for power supply unit for portable electronic devices, transportation and power generation.

Electrode reaction of PEMFC is divided into anode which hydrogen is oxidized and cathode reaction where water is generated by reducing oxygen. In the case of anode, the reaction rate is about 5 times faster than cathode's reaction. Therefore, It is essential that the development of the endothelial toxic catalyst can prevent the deactivation of the anode catalyst by poisoning of carbon monoxide and sulfur than the direction of increasing the catalyst activity.

Among the core materials that make up PEMFC, electrodes that undergo electrochemical reactions are used as expensive platinum catalysts, so the increase in system manufacturing cost is recognized as one of the major obstacles to commercialization. Therefore, to solve this problem, palladium, which is lower price than platinum and exhibits similar catalytic activity, is considered as a substitute. In addition, palladium is used as a hydrogen storage medium because of its strong adsorption capacity to hydrogen and is also used as a sensor and purification.

By synthesizing the metal sulfide nanostructures in the desired form, they can exhibit interesting properties for various electrochemical reactions. Surface metals and sulfur atoms can directly affect the interaction between reactive molecules and the catalyst surface. There is an effective strategy for adjusting the atomic distribution of sulfur and metal in metal sulfide nanoparticles to develop new catalysts with good electrocatalytic performance. Among the various methods for controlling the atomic ratio of metal and sulfur in the metal sulfide nanostructure, not only the control of the degree of sulfidation but also the synthesis of a specific crystal surface shows unique surface morphology and thus affects the catalytic properties.

Until now, palladium sulfide has been rarely studied in oxidation reactions. In fact, palladium sulfides have poor activity. This is due to the absence of the {100} crystal plane of the surface.

However, when partially sulfidation on the surface, the activity was improved. This is due to the change in the electronic structure of palladium due to partial sulfides.

Interestingly, when comparing the palladium sulfide nanocube and the palladium nanocube doped with sulfur other than Pd_{cube}/Pd-S/I, the palladium nanocube shows higher activity. This clearly shows that the sulfur content is very closely related to the ethanol oxidation activity of palladium. Metal chalcogenide (sulfide) catalysts doped with chalcogenides throughout the nanoparticles showed excellent catalytic activity in water splitting reactions, whereas for palladium sulfide, partial doping of the surface has a positive effect on the catalytic activity.

Index

Korean abstract	i
Abstract	iii
I. Introduction	1
II. Results and Discussion	4
III. Experimental Section	29
IV. Conclusion	32
V. Reference	33

I. Introduction

Metal nanoparticles (NPs) have attracted great attention because of their fascinating electronic, optical, and catalytic properties.¹⁻² The extraordinary behaviors of the different types of NPs are attributed to their discriminative physicochemical properties, which are closely associated with their size, composition, and surface morphology.³⁻⁴ In recent years, metal NPs with controlled shapes or morphologies have shown remarkable performances in electrocatalytic liquid fuel oxidation reactions for the anode of polymer electrolyte membrane fuel cell (PEMFC)(Figure 1).⁵⁻⁸ For example, concave Pt nanocrystals (NCs) exhibited enhanced electrocatalytic activities toward both oxidations of ethanol and formic acid than commercial Pt/C catalysts because of their high surface energy derived from well-defined shape.⁹ In addition, Xie and co-worker demonstrated that the electrocatalytic activity of cyclic pent-twinned Rh nanobranches with high percentage of {100} facets and large surface areas was higher than different shaped Rh NCs and Rh black catalysts.¹⁰ However, there are several limitations that hamper the practical application of these NPs based catalysts including insufficient catalytic activity and stability and high cost.¹¹⁻¹² In terms of inferior activity and stability, agglomeration and dissolution of NPs have been verified to be the critical factor to the catalysts failure.

Recently, shape-controlled Pd and Pd-based NPs have been accepted important catalysts comparable with Pt NPs for liquid fuel oxidation reactions due to not only their superb catalytic activity but also high stability.¹³⁻¹⁵ For example, cubic Pd NPs enclosed of {100}-bounded surface showed superior electrochemical fuel oxidation activity and stability than different types of Pd NPs because the oxidation of liquid fuel is largely dependent on the distinctive surface morphology.¹⁶⁻¹⁸ Notably, Cai and co-worker reported that cubic Pd NPs are the most suitable catalysts compared with their counterparts enclosed of different facets to enhance ethanol electrooxidation. Despite of the improved catalytic performance of Pd NPs with controlled shapes, the levels of activity and stability are still low for the commercialization standards. Therefore, it is necessary to develop novel strategy for improving Pd based catalysts.

Controllable synthesis of metal sulfide nanostructures with desired morphology is of great importance due to their interesting properties for various electrochemical reactions.¹⁹⁻²⁰ The catalytic property of these catalysts can be improved by tuning their composition ratios

between metal and sulfur.²¹⁻²³ Accordingly, many researches have focused on adjusting the stoichiometry of the nanostructure to achieve the enhanced performance in electrocatalytic reactions.²⁴⁻²⁶ Of various strategies for controlling the atomic ratio of metal and sulfur in metal sulfide nanostructures, since both surface metal and sulfur atoms can directly influence on interaction between reactive molecules and surface of catalysts, tuning the atomic distribution of sulfur and metal on the metal sulfide NPs by controlling the degree of sulfidation is an effective strategy for developing novel catalysts with superb electrocatalytic performance. In addition to degree of sulfurizing, shape-controlled metal sulfide NPs composed of particular facets influence on catalytic properties due to their distinctive surface morphologies.²⁷⁻²⁹ For example, Feng et al. showed that {210} high-index facet of Ni₃-S₂ NPs is effective active-site for electrochemical water splitting because adsorption of intermediates on the catalyst surface can be promoted on the high-index facets.³⁰ Collectively, inspired by the previous findings, regulating the both degree of sulfidation and shape of Pd sulfide NPs can lead the enhanced catalytic performances toward electrocatalysis reactions. However, unlike Ni-S, Co-S, and other metal-sulfide catalysts, studies over electrocatalytic performance of Pd sulfide NPs with well-defined shape and composition have not been fully investigated due to difficulty to simultaneously controlling both sulfur distributions and shape of nanostructure despite potentially great impact on catalysis.

Here, we present a facile synthetic method for cubic and octahedral Pd sulfide NPs by sulfurizing preformed cubic and octahedral Pd NPs. The fine controlling of the degree of sulfidation through manipulation of sulfur concentration is key lever for synthesis of various Pd sulfide NPs with different sulfur distributions. The different Pd sulfide NPs showed distinctive electrocatalytic properties toward ethanol oxidation reaction (EOR) depending on shape and sulfur distribution. Significantly, owing to the partially sulfurized Pd/Pd-S and {100}-bounded surface, Pd_{cube}/Pd-S/I NPs exhibited superior catalytic activity and stability toward EOR than their Pd sulfide NP counterparts with different sulfur distributions and shapes, pristine Pd NPs, and commercial Pd/C catalysts.

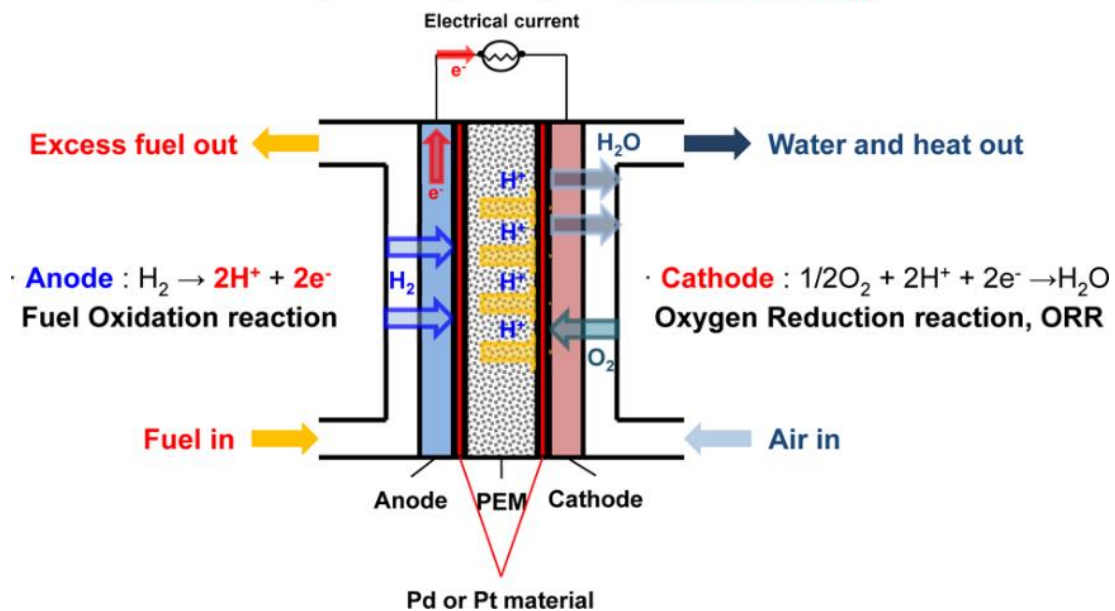


Figure 1. Schematic of PEMFCs

II. Result and Discussion

Palladium sulfide nanoparticles

Figure 2 illustrates the synthesis of shape-controlled Pd sulfide NPs with different sulfur distributions. For preparing the Pd sulfide NPs, cubic and octahedral Pd NPs were first produced by using wet-chemical methods. The edge lengths of cubic and octahedral Pd NPs are 17.3 ± 1.5 and 23.3 ± 1.0 nm, respectively (Figure 3). The scanning electron microscopy (SEM) and transmission electron microscopy (TEM) images show their well-defined cubic and octahedral morphologies. For the preparation of cubic Pd sulfide NPs with various sulfur distributions, different concentrations of Na_2S as a sulfur source were injected into reaction mixtures including cetyltrimethyl ammonium (CTAC) and cubic Pd NPs. The reaction mixture was then heated until $100\text{ }^\circ\text{C}$ and maintained at the same temperature for 10 min. Similarly, octahedral Pd NPs were used instead of cubic Pd NPs for preparing the octahedral Pd sulfide NPs under identical experimental conditions to those employed in the synthesis for cubic Pd sulfide NPs.

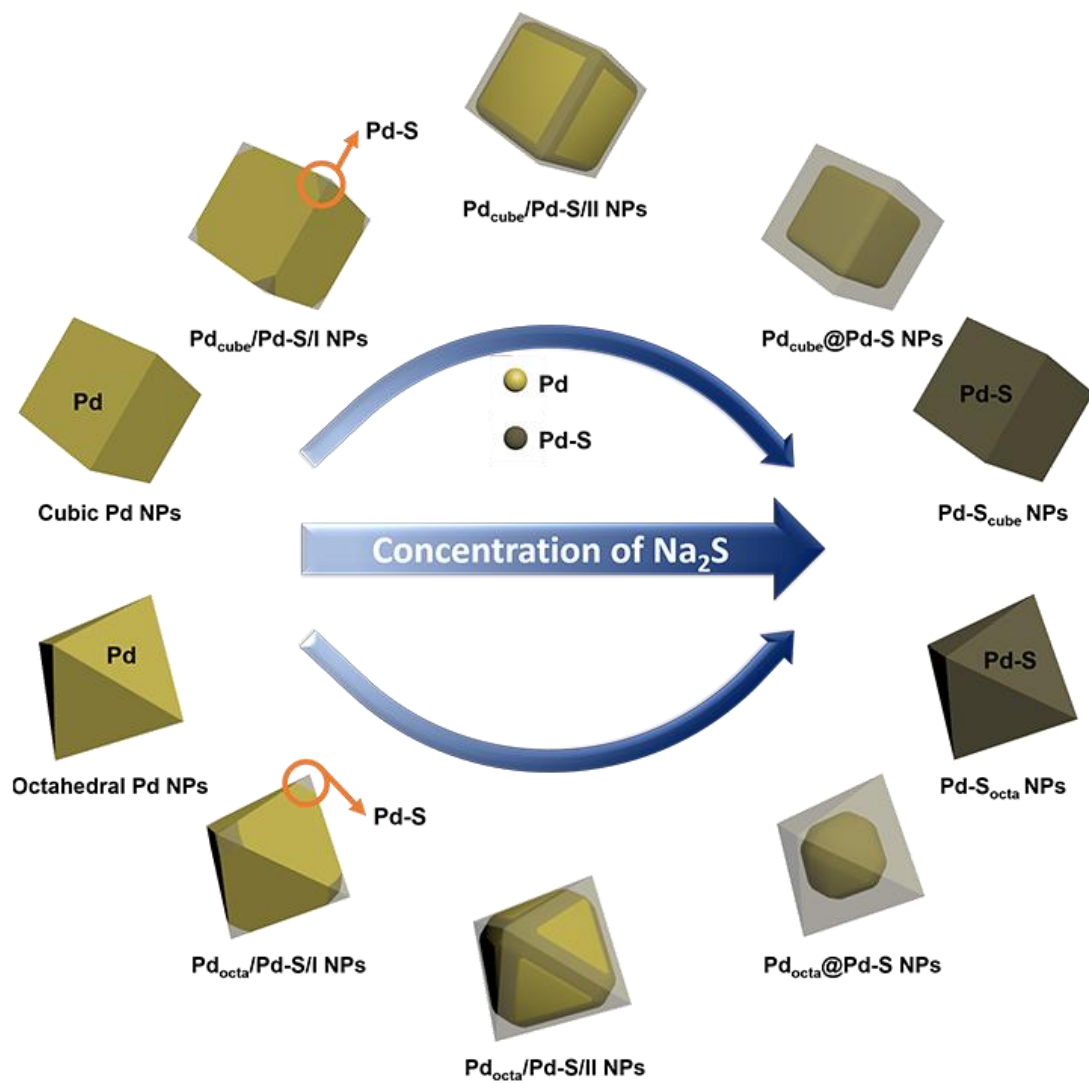


Figure 2. Schematic illustration of the synthetic strategy of various Pd sulfide NPs.

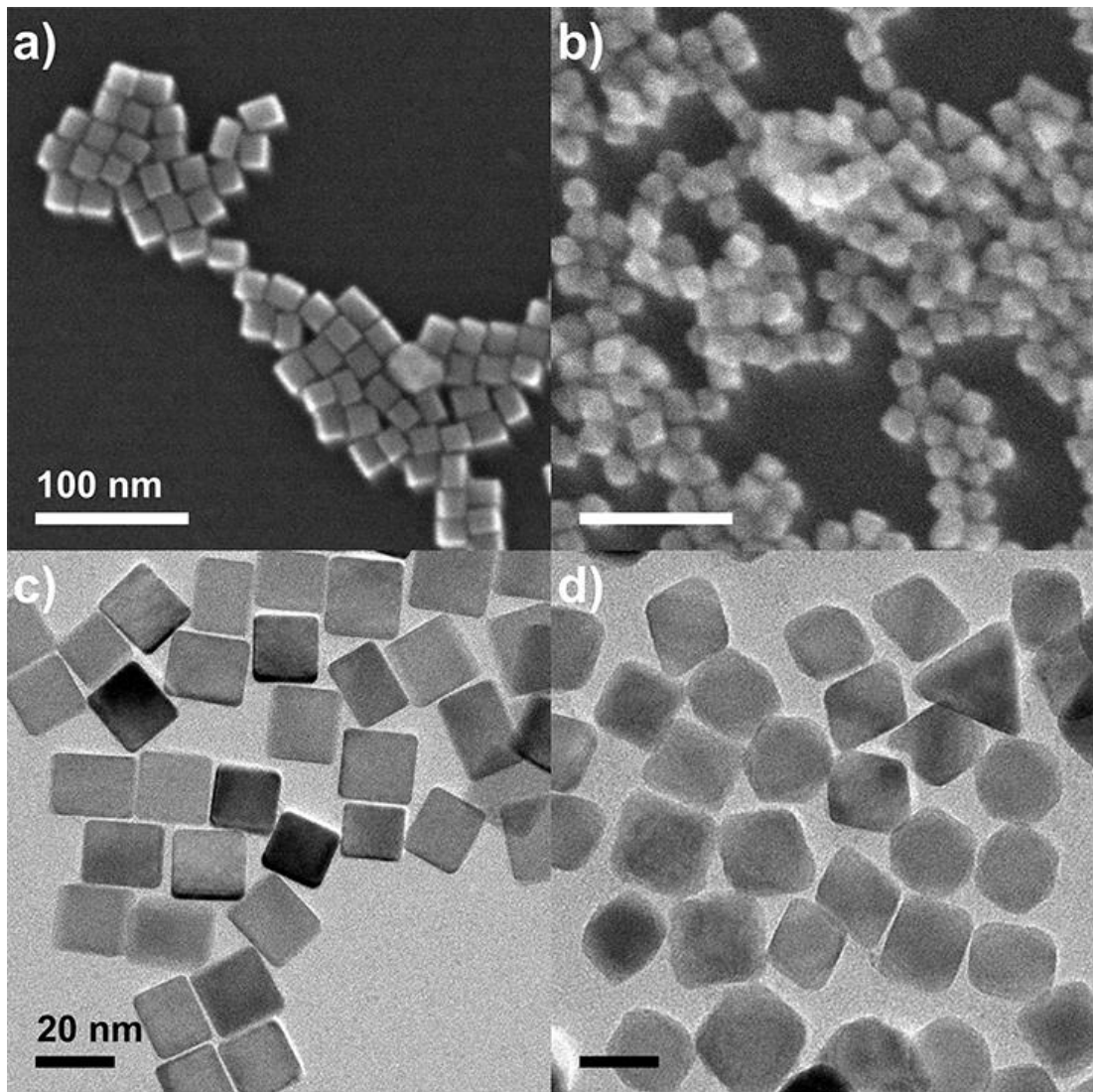


Figure 3. SEM (a,b) and TEM (c,d) images of cubic Pd (a,c) and octahedral Pd NPs (b,d).

As shown in the typical TEM images, the sulfurized regions on the cubic Pd sulfide NPs can be discriminated from the pure Pd region due to transformation of crystalline Pd to amorphous Pd-S nature and difference in electron-scattering efficiencies between Pd and Pd-S (Figure 4a-d and 5a-d). The cubic Pd sulfide NPs with different sulfur distributions were referred to as Pd_{cube}/Pd-S/I, Pd_{cube}/Pd-S/II, Pd_{cube}@Pd-S, and Pd-S_{cube} NPs, which have been produced by adding 5, 10, 30, and 100 mM of Na₂S, respectively. Although Pd-S_{cube} NPs showed slightly rounded edges and vertices, no severe deformation of cubic shape for other cubic Pd sulfide NPs was observed after sulfidation. The extent of sulfidation in as-prepared Pd sulfide NPs was determined from high-resolution TEM (HRTEM) images. With careful observation, amorphous and bright contrast spots were observed in the partial regions of the Pd_{cube}/Pd-S/I NPs (Figure 4a), signifying that partially sulfurized Pd/Pd-S surface are formed by selective sulfidation in low concentration of Na₂S. The Pd_{cube}/Pd-S/II NPs with more sulfurized surfaces were produced by increasing the concentration of Na₂S from 5 to 10 mM. Figure 4b shows that amorphous regions with bright contrast on surfaces of the Pd_{cube}/Pd-S/II NPs are expanded compared with the Pd_{cube}/Pd-S/I NPs. The Fourier transform (FFT) patterns of two types of Pd sulfide NPs obtained from sulfurized and Pd core regions along the [001] zone axis clearly show the amorphous and crystalline nature, respectively. This indicates that crystalline nature of pure Pd is converted to amorphous Pd-S by sulfidation. In contrast to Pd_{cube}/Pd-S/I and Pd_{cube}/Pd-S/II NPs, when the concentration of Na₂S was increased to 30 mM, the Pd_{cube}@Pd-S NPs with entirely sulfurized surfaces were produced, of which amorphous Pd-S shell thickness is 3.2 ± 0.2 nm (Figure 4c). Furthermore, injection of 100 mM of Na₂S fully converted the crystalline cubic Pd NPs to amorphous Pd-S_{cube} NPs (Figure 4d and Figure 5d). Similarly, performing the sulfidation by using 5, 10, 30, and 100 mM of Na₂S with octahedral Pd NPs instead of cubic Pd NPs produces Pd_{octa}/Pd-S/I, Pd_{octa}/Pd-S/II, Pd_{octa}@Pd-S, and Pd-S_{octa} NPs, respectively (Figures 4e-h and 5e-h), which have analogous sulfur distributions with cubic Pd sulfide NPs. For the Pd-S_{octa} NPs, sulfidation was fully proceeded throughout the NPs (Figure 1h). Based on the findings, we found that this sulfurizing approach allow the diffuse of sulfur into the interior of the Pd NPs maintaining their initial shapes and higher concentration of Na₂S promotes the sulfidation of Pd NPs.

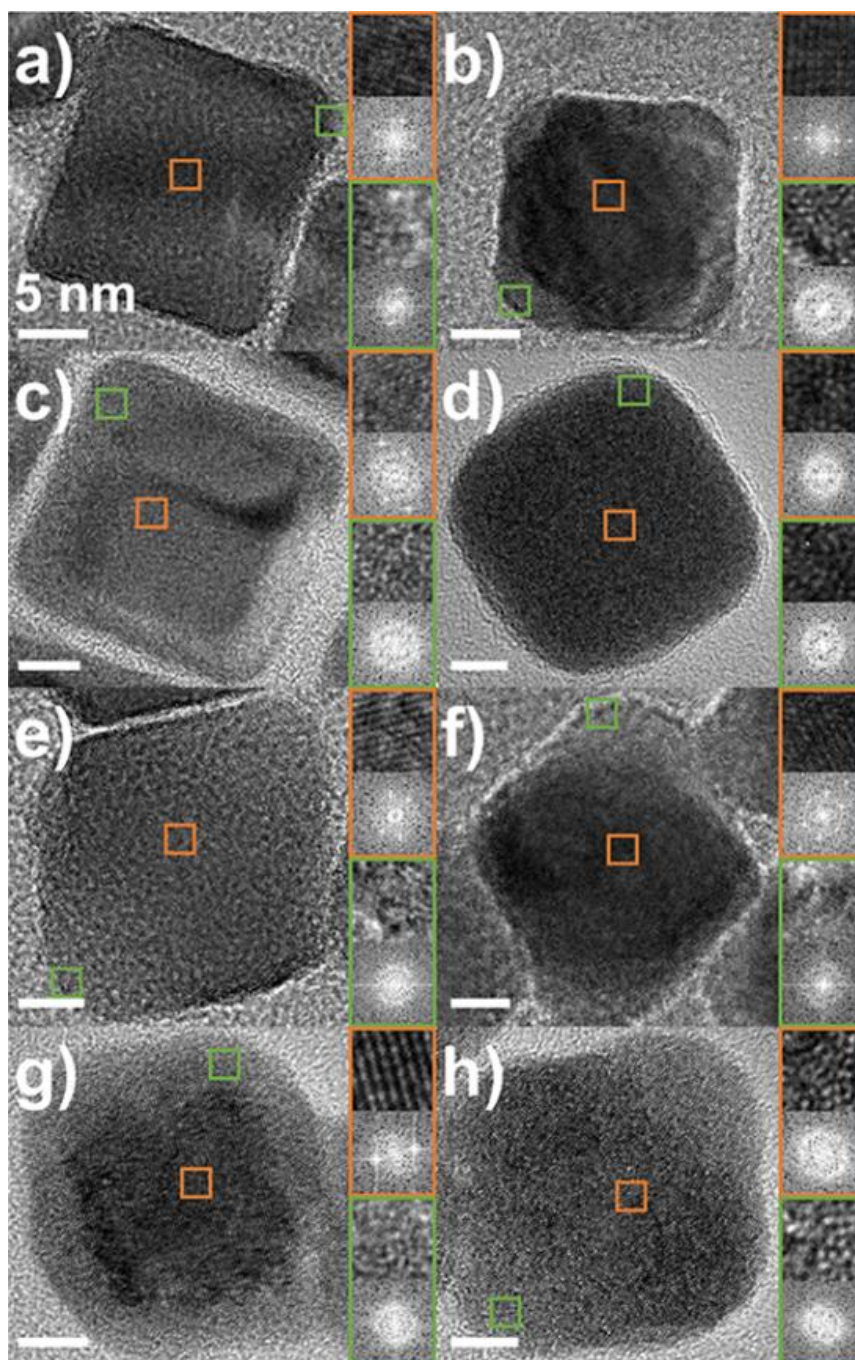


Figure 4. TEM images of (a) Pd_{cube}/Pd-S/I, (b) Pd_{cube}/Pd-S/II, (c) Pd_{cube}@Pd-S, (d) Pd-S_{cube}, (e) Pd_{octa}/Pd-S/I (f) Pd_{octa}/Pd-S/II (g) Pd_{octa}@Pd-S and (h) Pd-S_{octa} NP. The high-resolution TEM images and corresponding FFT patterns for the central regions (orange squares) and edge regions (green squares) of different Pd sulfide NPs.

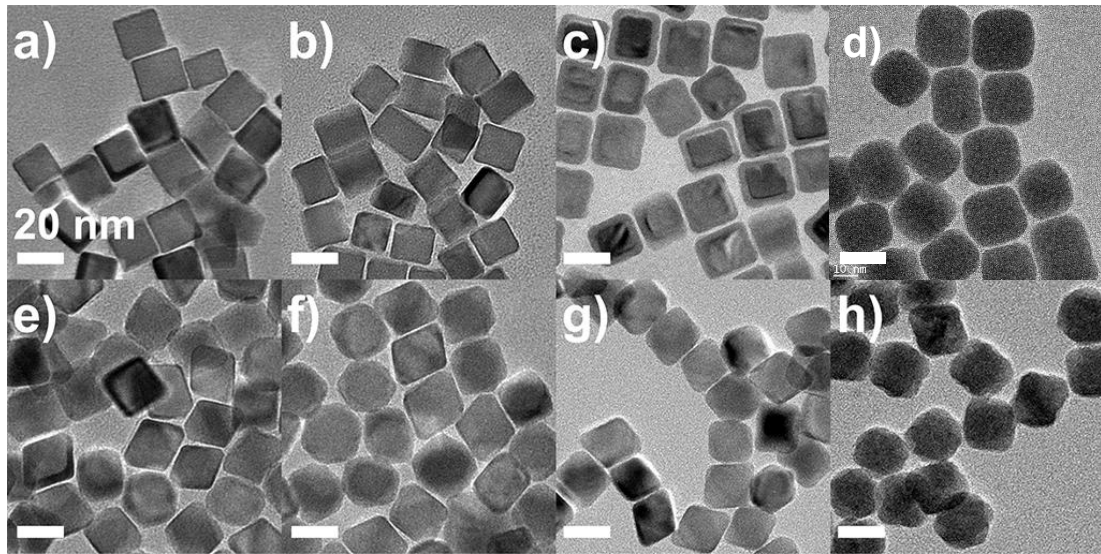


Figure 5. Low-magnification TEM images of Pd_{cube}/Pd-S/I, (b) Pd_{cube}/Pd-S/II, (c) Pd_{cube}@Pd-S, (d) Pd-S_{cube}, (e) Pd_{octa}/Pd-S/I (f) Pd_{octa}/Pd-S/II (g) Pd_{octa}@Pd-S and (h) Pd-S_{octa} NPs.

The conversion of crystalline structures was further verified by X-ray diffraction (XRD) measurement (Figure 6). The Pd_{cube}/Pd-S/I and Pd_{cube}/Pd-S/II NPs show similar XRD patterns with that of pure cubic Pd NPs, demonstrating that small partial regions were selectively sulfurized. The XRD results of Pd_{cube}@Pd-S NPs also show the diffraction peaks of fcc Pd reference due to existence of Pd core. In contrast, XRD pattern was disappeared for the Pd-S_{cube} NPs implying an amorphous nature due to full conversion of Pd to Pd-S, which highly corresponds with TEM observation. Furthermore, the crystalline sizes of the NPs were calculated by using Scherrer equation based on the XRD patterns, which exhibited the 17.2, 16.9, 16.2, and 13.7 nm of crystalline sizes for the cubic Pd, Pd_{cube}/Pd-S/I, Pd_{cube}/Pd-S/II, and Pd_{cube}@Pd-S, respectively. This highly corresponds with decreasing Pd core size in TEM images of the NPs.

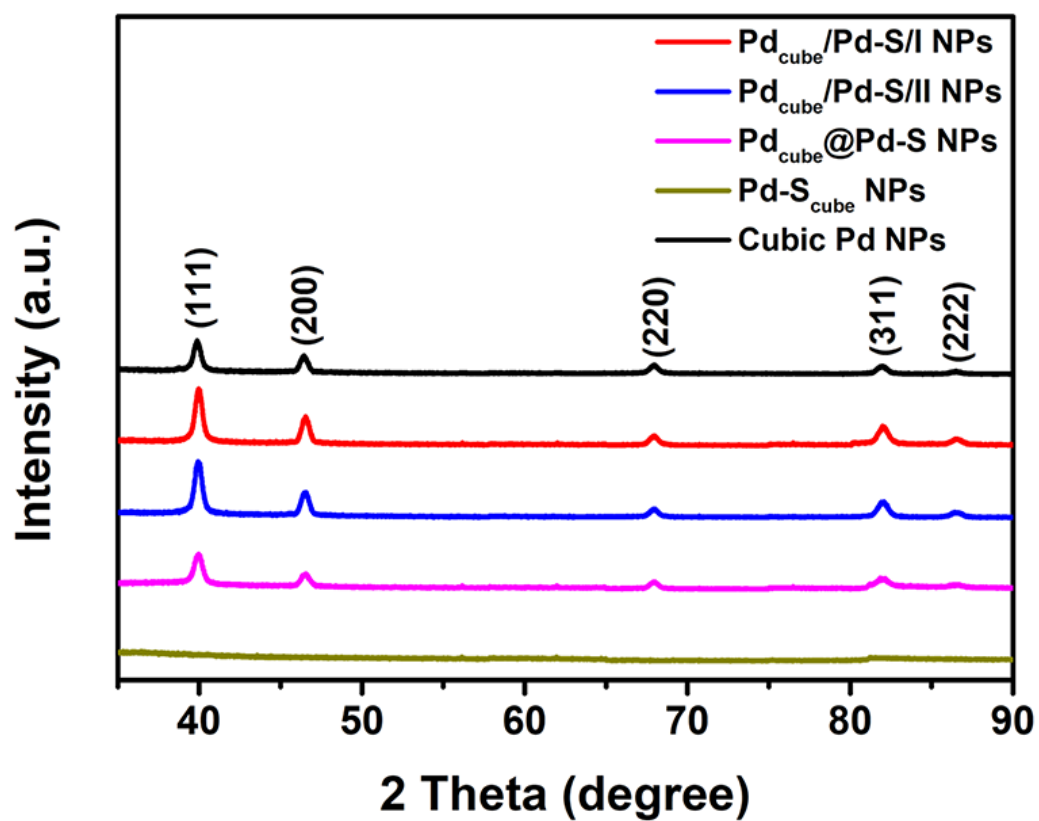


Figure 6. XRD patterns of cubic Pd sulfide and cubic Pd NPs.

To investigate the sulfur distribution of the NPs, the compositional structures of different cubic Pd sulfide NPs were obtained by high-angle annular dark-field scanning TEM (HAADF-STEM) and corresponding energy dispersive X-ray spectroscopy (EDS) measurement. The HAADF-STEM-EDS mapping images of the Pd_{cube}/Pd-S/I, Pd_{cube}/Pd-S/II, Pd_{cube}@Pd-S, and Pd-S_{cube} NPs show the different sulfur distributions in the nanostructures (Figure 7). The partially sulfurized surfaces for Pd_{cube}/Pd-S/I and Pd_{cube}/Pd-S/II NPs were confirmed by intense sulfur signals appearing in the edges compared to plane regions (Figure 7a,b), while similar intensities of sulfur signal were observed on the all shell regions of the Pd_{cube}@Pd-S NPs, implying the formation of Pd-S shells (Figure 7c). For Pd-S_{cube} NPs, the evenly distributed sulfur signals over the NPs indicate the full transformation of cubic Pd NPs to Pd-S NPs (Figure 7d).

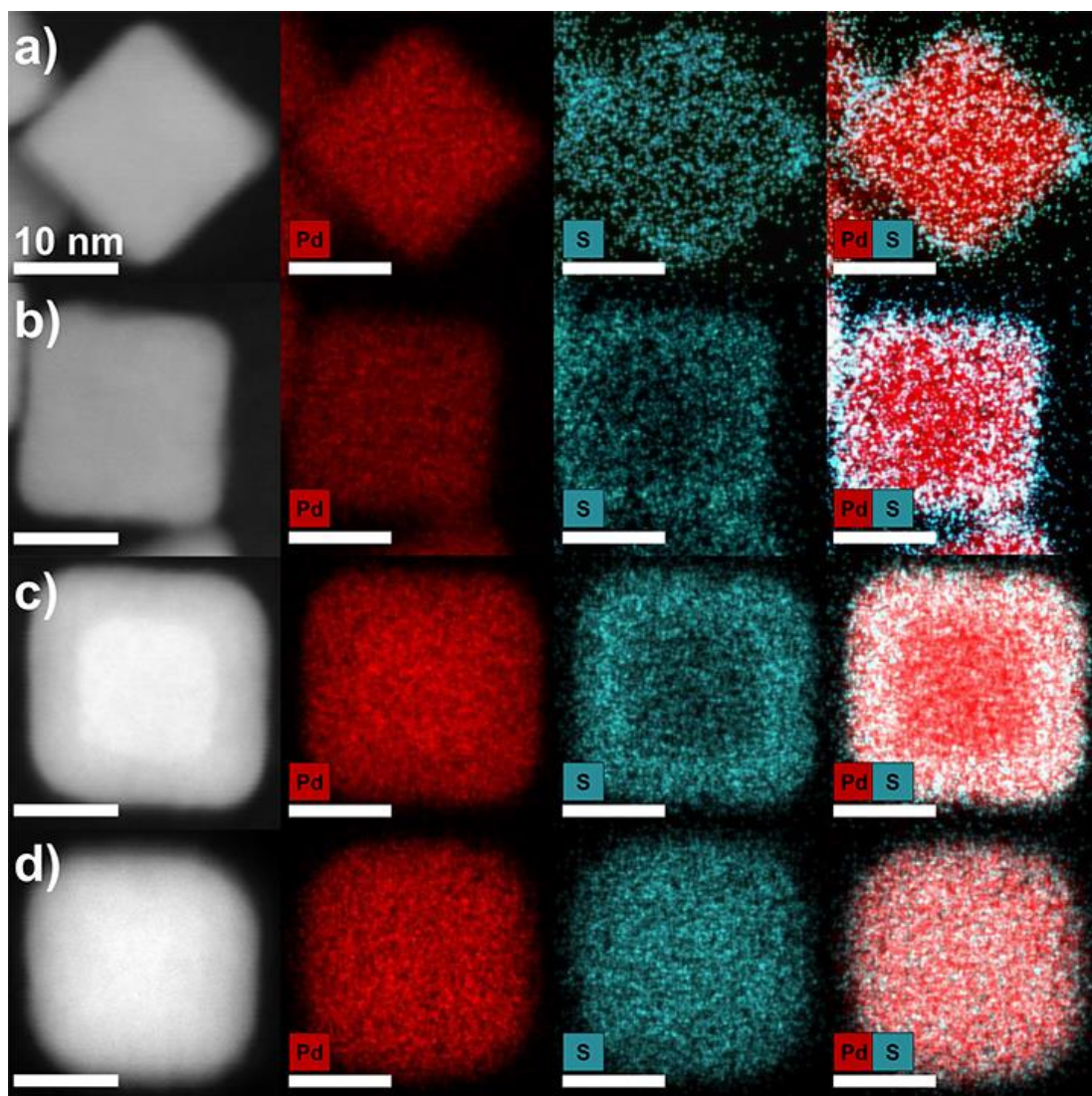


Figure 7. HAADF-STEM images and corresponding EDS elemental mapping images of (a) Pd_{cube}/Pd-S/I, (b) Pd_{cube}/Pd-S/II, (c) Pd_{cube}@Pd-S, and (d) Pd-S_{cube} NPs. The scale bars in a-d indicate 10 nm.

To further elucidate the different sulfur distributions of the NPs, Pd was selectively etched from various Pd sulfide NPs in acidic solution (5 M of HNO_3), which is possible because of higher chemical stability of Pd-S than Pd.^x When the Pd sulfide NPs with partially sulfurized surfaces such as Pd_{cube}/Pd-S/I and Pd_{cube}/Pd-S/II NPs were treated with acidic solution, broken nanostructures were observed (Figure 8a,b and Figure 9a,b). This demonstrates that partial edge areas of cubic Pd NPs are dominantly converted to Pd-S in low concentration of Na_2S . In the case of Pd_{cube}@Pd-S NPs after acid treatment, majority of products was cubic hollow structures due to well-preserved Pd-S shell (Figure 8c and Figure 9c). Pd-S NPs maintained their initial morphology after the treatment (Figure 8d and Figure 9d). These clearly verify the different sulfur distributions of the Pd sulfide NPs. The results highly correlated with above TEM and HAADF-STEM-EDS analysis indicate the importance of the manipulation of the concentration of sulfur source in the production of Pd sulfide NPs with well-defined sulfur distribution.

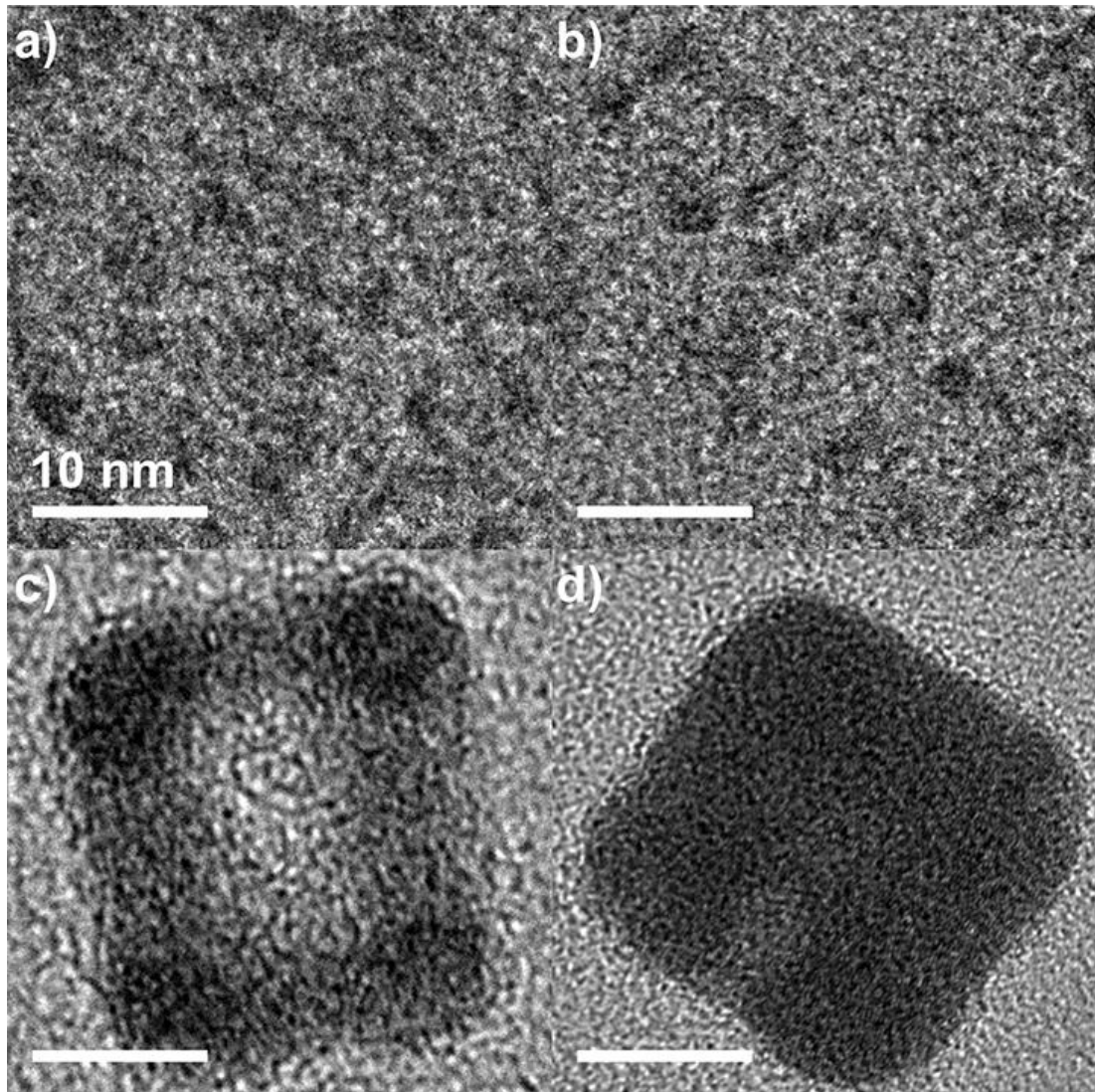


Figure 8. TEM images of (a) Pd_{cube}/Pd-S/I, (b) Pd_{cube}/Pd-S/II, (c) Pd_{cube}@Pd-S, and (d) Pd-S_{cube} NPs after etching treatment.

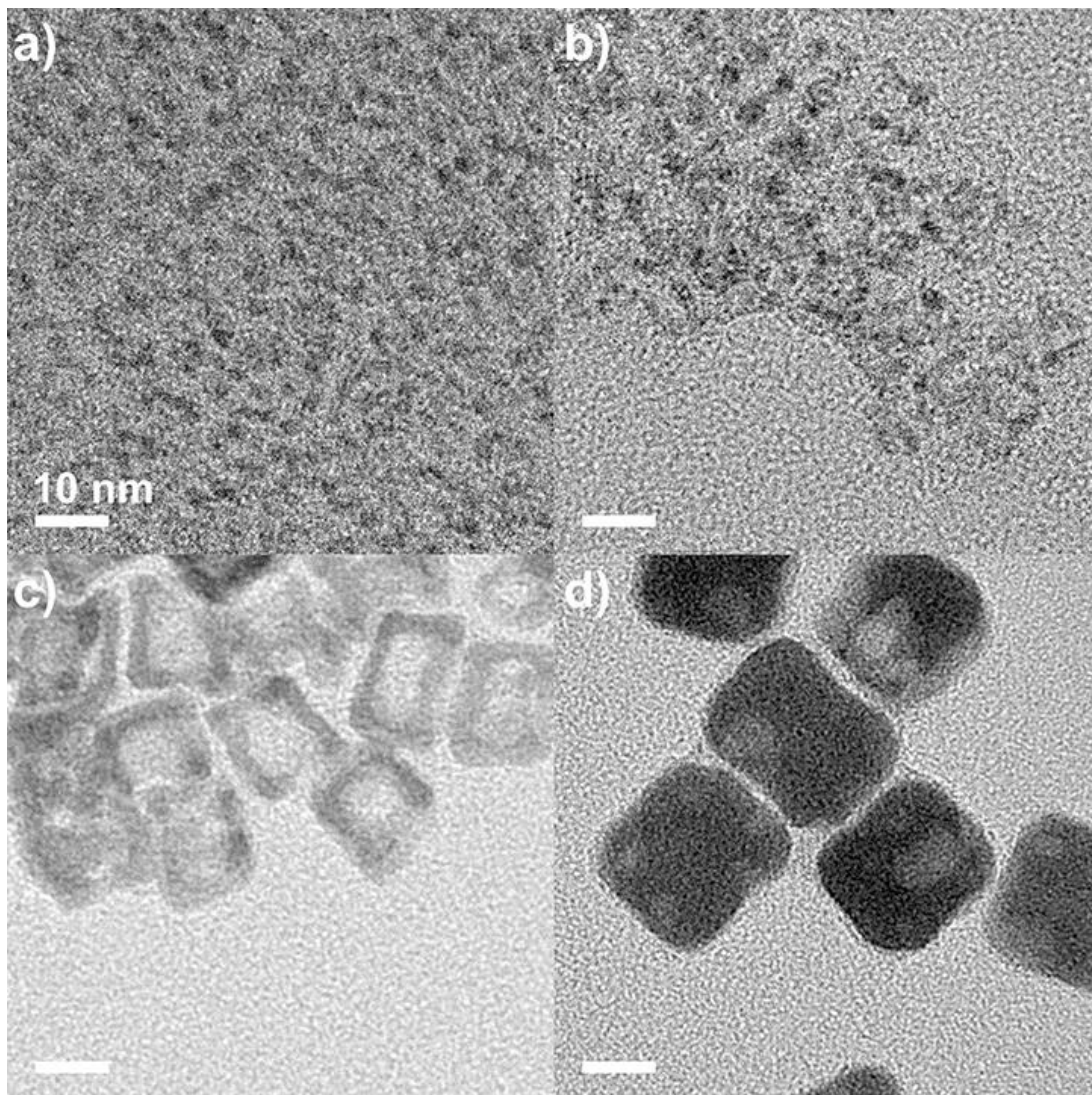


Figure 9. Low-magnification TEM images of (a) Pd_{cube}/Pd-S/I, (b) Pd_{cube}/Pd-S/II, (c) Pd_{cube}@Pd-S, and (d) Pd-S_{cube} NPs after etching treatment.

To evaluate the effect of sulfur distribution on the electrocatalytic activity of Pd sulfide NPs, catalytic activities of various cubic Pd sulfide NPs, Pd_{cube}/Pd-S/I, Pd_{cube}/Pd-S/II, Pd_{cube}@Pd-S, and Pd-S_{cube} NPs, were measured toward EOR in alkaline media on behalf of all Pd sulfide NPs prepared (Figure 10). Before the electrochemical experiments, all cubic Pd sulfide NPs were uniformly anchored on carbon support by sonicating the aqueous mixture including the NPs and carbon support. The catalysts deposited on carbon support were further cleaned with ethanol and water to remove the chemicals adsorbed on the surfaces of the catalysts. Figure 10a shows cyclic voltammograms (CVs) of different catalysts in Ar-saturated 0.5 M KOH solution at a scan rate of 50 mV s⁻¹. The electrochemically active surface areas (ECSAs) of the Pd_{cube}/Pd-S/I, Pd_{cube}/Pd-S/II, Pd_{cube}@Pd-S, and Pd-S_{cube} NPs were obtained to be 24.5, 20.2, 21.2, and 20.7 m² g⁻¹, respectively, based on the Coulombic charges for oxygen desorption in the CVs of the catalysts. Figure 5b shows CVs of glassy carbon electrodes (GCE) modified with the catalysts measured in Ar-saturated 0.5 M KOH + 1 M ethanol solution at a scan rate of 50 mV s⁻¹. In the CVs, well-defined oxidation peaks originated from oxidation of ethanol were clearly identified. The catalytic activity of the Pd_{cube}/Pd-S/I NPs was much larger compared with those of other catalysts. The mass activities normalized by amount of Pd and S of the Pd_{cube}/Pd-S/I NPs is 2581.0 mA mg⁻¹, roughly 1.5, 2.7, and 3.3 folds higher than those of Pd_{cube}/Pd-S/II (1681.0 mA mg⁻¹), Pd_{cube}@Pd-S (973.7 mA mg⁻¹), and Pd-S_{cube} NPs (793.9 mA mg⁻¹), respectively (Figure 10b,d). In addition, the catalytic activities of the catalysts evaluated from the current densities, normalized to the ECSA, exhibited an analogous trend. As shown in Figure 10c,d, the Pd_{cube}/Pd-S/I NPs also exhibited the most pronounced specific activity, 10.5 mA cm⁻², roughly 1.3, 2.3, and 2.8 times higher than those of Pd_{cube}/Pd-S/II (8.3 mA cm⁻²), Pd_{cube}@Pd-S (4.6 mA cm⁻²), and Pd-S_{cube} NPs (3.8 mA cm⁻²), respectively. It is apparent that the catalytic activity of the Pd sulfide NPs for EOR obviously depends on their degree of sulfidation. These results imply that partially sulfurized Pd-S surface of the Pd_{cube}/Pd-S/I NPs can improve the electrocatalytic activity, whereas Pd-S shell formed by fully sulfurizing the Pd surface deteriorates active Pd surface atoms due to their amorphous structures. Based on these findings, the Pd_{cube}/Pd-S/I NPs were chosen for further studying the electrochemical properties depending on their surface structures.

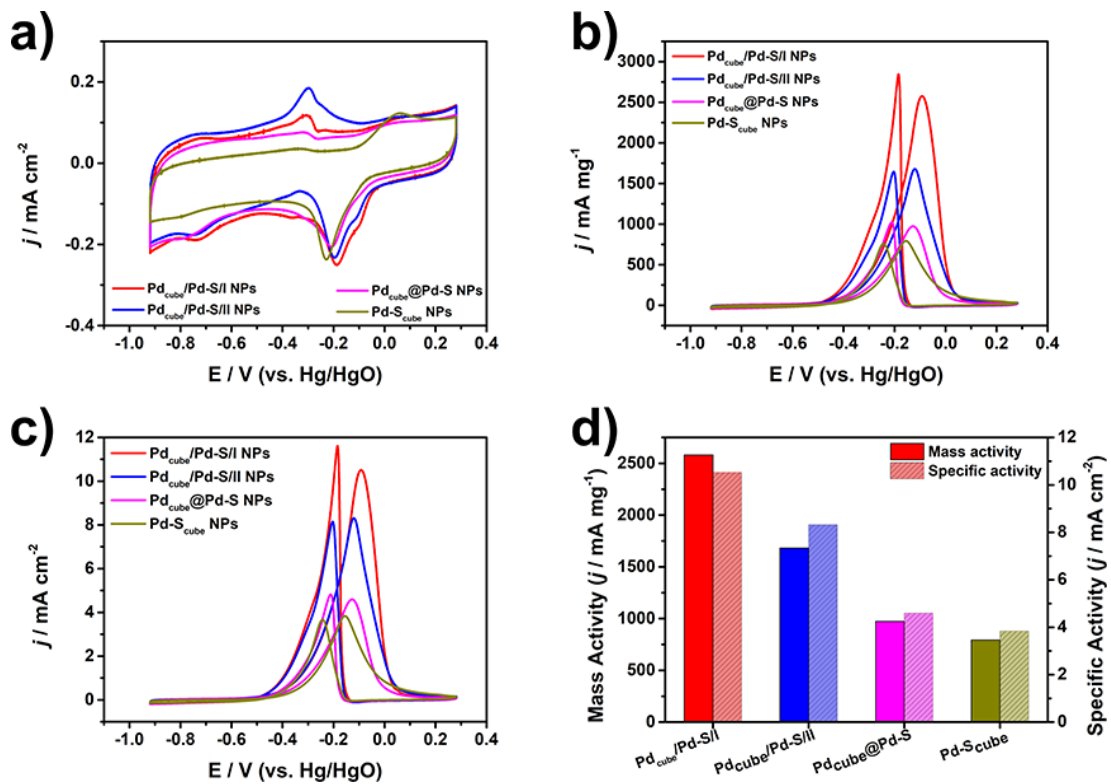


Figure 10. CVs of the Pd_{cube}/Pd-S/I, Pd_{cube}/Pd-S/II, Pd_{cube}@Pd-S, and Pd-S_{cube} NPs on GCE in (a) 0.5 M KOH and (b,c) 0.5 KOH + 1 M ethanol. Current values were normalized with respect to (b) mass and (c) the ECSA of catalysts. (d) Catalytic activities of various catalysts for the EOR.

For investigating the influence of surface atomic arrangement of the NPs on their catalytic properties, the electrochemical properties of the Pd_{cube}/Pd-S/I NPs as well as Pd_{octa}/Pd-S/I NPs, cubic Pd NPs, and octahedral Pd NPs were examined toward EOR and further benchmarked against the commercial Pd/C catalyst. The ECSAs of the Pd_{cube}/Pd-S/I NPs, Pd_{octa}/Pd-S/I NPs, cubic Pd NPs, octahedral Pd NPs, and commercial Pd/C catalysts calculated from CVs shown in Figure 11a were 24.5, 22.0, 22.9, 21.3, and 38.3 m² g⁻¹, respectively, which show no significant changes of ECSA of the Pd sulfide NPs compared to those of pristine cubic and octahedral Pd NPs, corroborating the shape preservation of sulfurized catalysts. The CVs obtained for the EOR of the catalysts revealed the typical electrochemical ethanol oxidation peaks in forward and backward scans (Figure 11b,c). The mass activity of Pd_{cube}/Pd-S/I NPs was higher than the other catalysts, further confirming their enhanced electrocatalytic activities in specific activity (Figure 11b-d). The mass activities of the catalysts follow the order of Pd_{cube}/Pd-S/I NPs (2581.0 mA mg⁻¹) > cubic Pd NPs (2202.3 mA mg⁻¹) > Pd_{octa}/Pd-S/I NPs (1547.0 mA mg⁻¹) > commercial Pd/C (1302.0 mA mg⁻¹) > octahedral Pd NPs (1250.0 mA mg⁻¹), respectively. The specific activities of Pd_{cube}/Pd-S/I NPs, Pd_{octa}/Pd-S/I NPs, cubic Pd NPs, octahedral Pd NPs, and commercial Pd/C were 10.5, 9.6, 7.0, 5.9, and 3.4 mA cm⁻², respectively. Importantly, the catalytic activities of the Pd_{cube}/Pd-S/I NPs and cubic Pd NPs were larger than those of catalysts with octahedral morphology. This reveals that {100}-bounded surface originated from cubic shape is favorable to improve the catalytic performance for EOR than the {111}-bounded surface from octahedral shape. On the other hand, when catalytic activities of the Pd_{cube}/Pd-S/I and Pd_{octa}/Pd-S/I NPs are compared with those of their pristine Pd NP counterparts like cubic and octahedral Pd NPs, respectively, the Pd sulfide NPs containing both Pd and Pd-S surfaces exhibited higher catalytic activities than pristine Pd NP counterparts, respectively. Taken together, these demonstrate that the significant enhancement in the catalytic activities of the Pd_{cube}/Pd-S/I and Pd_{octa}/Pd-S/I NPs than those of the cubic and octahedral Pd NPs can be ascribed to synergistic effects by co-existence of Pd and Pd-S surfaces.

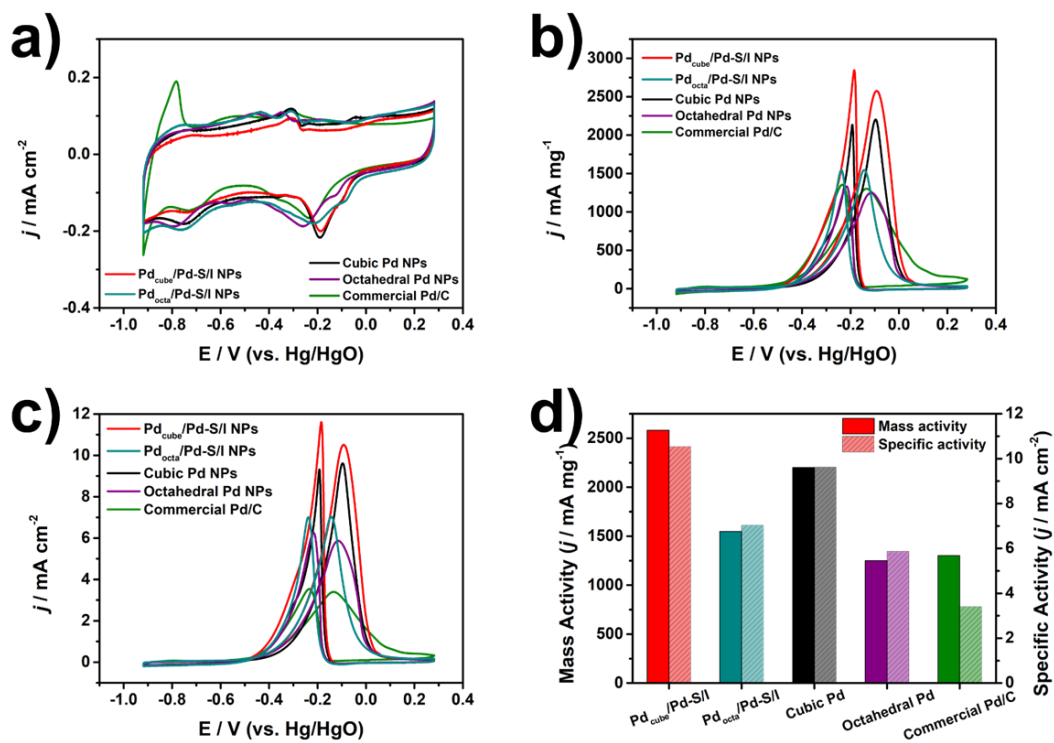


Figure 11. CVs of the Pd_{cube}/Pd-S/I NPs, Pd_{octa}/Pd-S/I NPs, cubic Pd NPs, octahedral Pd NPs, and commercial Pd/C on GCE in (a) 0.5 M KOH and (b,c) 0.5 KOH + 1 M ethanol. Current values were normalized with respect to (b) mass and (c) the ECSA of catalysts. (d) Catalytic activities of various catalysts for the EOR.

In alkaline media, ethanol can be oxidized to CO_2 on Pd surfaces through two pathways named as to poisoning intermediate (CO) and reactive intermediate pathways (Figure 12). The adsorption of poisoning intermediates like CO formed via CO intermediate pathway can disturb EOR by reducing active Pd surface sites, and thus it can be assumed that reactive intermediate pathway is more desirable for improving EOR activity. The higher catalytic activities of the $\text{Pd}_{\text{cube}}/\text{Pd-S/I}$ and $\text{Pd}_{\text{octa}}/\text{Pd-S/I}$ NPs than cubic and octahedral Pd NPs may be attributed the modified electronic structures of partially sulfurized Pd/Pd-S surfaces. X-ray photo-electron spectroscopy (XPS) was conducted to examine the change of the electronic structures of Pd in the $\text{Pd}_{\text{cube}}/\text{Pd-S/I}$ and $\text{Pd}_{\text{octa}}/\text{Pd-S/I}$ NPs. Figure 13a,b shows that binding energies for Pd 3d core-level of the $\text{Pd}_{\text{cube}}/\text{Pd-S/I}$ NPs shifted to lower values compared with those of cubic Pd NPs. For example, the Pd $3d_{5/2}$ and Pd $3d_{3/2}$ binding energies of the $\text{Pd}_{\text{cube}}/\text{Pd-S/I}$ NPs were 335.85 and 341.75 eV, while those of the cubic Pd NPs were 336.05 and 341.35 eV, respectively. Similarly, when binding energies for Pd core-level of $\text{Pd}_{\text{octa}}/\text{Pd-S/I}$ NPs are compared with those of the octahedral Pd NPs, analogous trend was also observed (Figure 13c,d). Based on the XPS results, we speculated that modified electronic structures of Pd in the Pd sulfide NPs can efficiently promote the electrochemical ethanol oxidation via reactive intermediate pathway than CO pathway, because decreased binding energy for Pd can facilitate the oxidation of intermediate such as acetate (COCH_3) to CO_2 than CO. This results in enhancement of EOR activities of the Pd sulfide NPs compared with pristine Pd NPs.

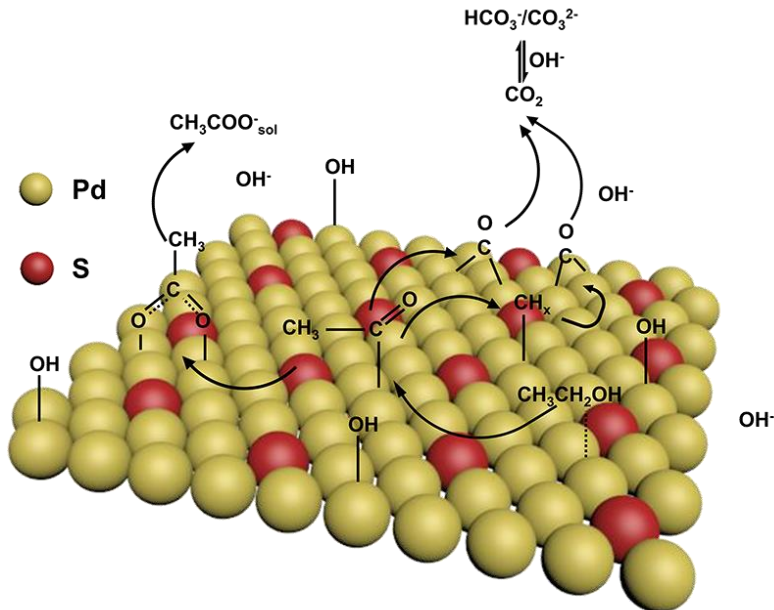
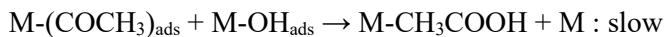
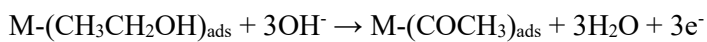
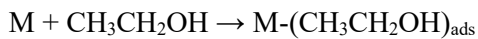
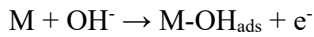


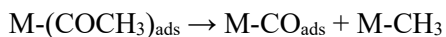
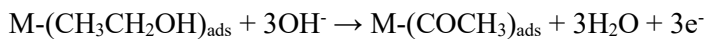
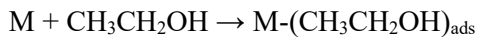
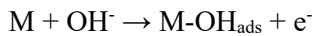
Figure 12. Schematic illustration of the EOR in alkaline media via the reactive intermediate and CO pathways.

It has been generally accepted that the EOR on metal (M) surfaces in alkaline media proceeds via the following 1) reactive intermediate and/or 2) poisoning intermediate (CO) pathway.

1) Reactive intermediate pathway:



2) Poisoning intermediate (CO) pathway:



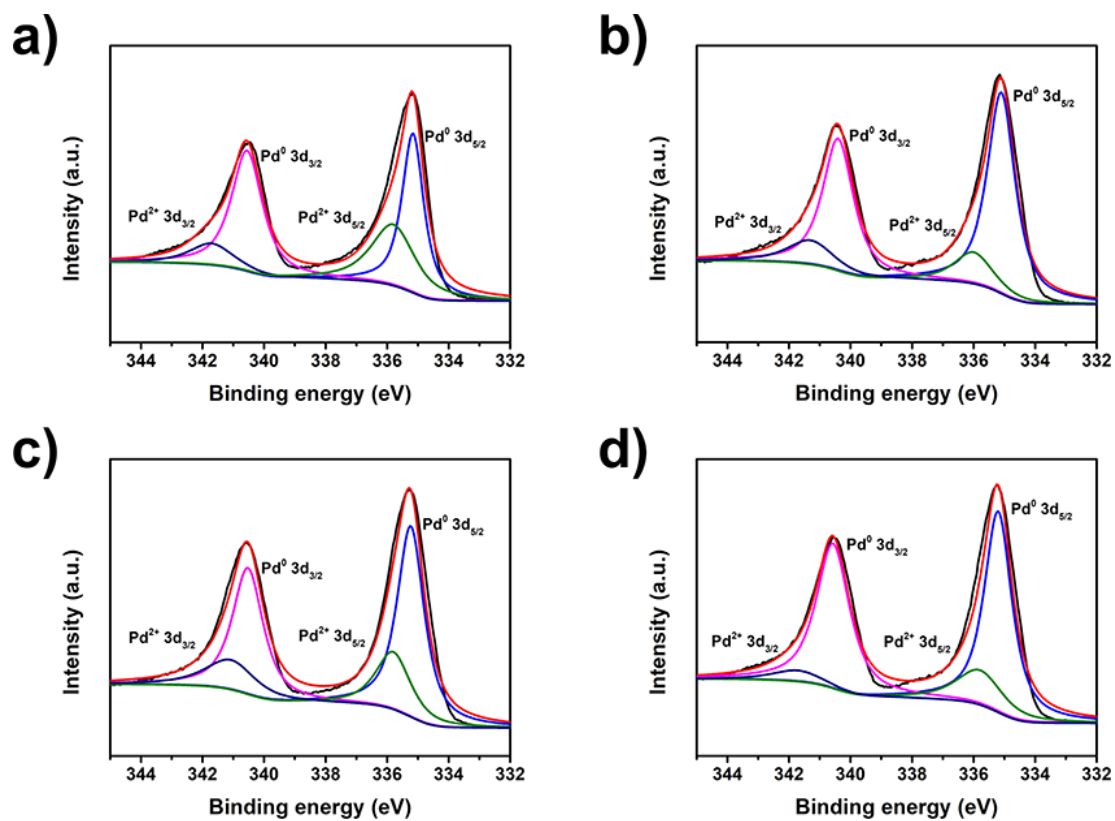


Figure 13. XPS spectra for Pd 3d of (a) Pd_{cube}/Pd-S/I, (b) cubic Pd, (c) Pd_{octa}/Pd-S/I, and (d) octahedral Pd NPs.

The eliminating the poisoning intermediates such as CO adsorbed on Pd surface is also important for improving EOR performance. Compared with the catalysts including octahedral Pd NPs such as Pd_{octa}/Pd-S/I and octahedral Pd NPs, higher catalytic activities of the Pd_{cube}/Pd-S/I and cubic Pd NPs can be attributed to their more efficient CO removal capabilities by {100}-bounded Pd surface. To demonstrate the differences of CO removal capability, CO stripping experiments were carried out with the catalysts. As shown in Figure 14a, current peak for CO oxidation in CO-stripping voltammogram of the Pd_{cube}/Pd-S/I NPs was observed at relatively negative potential compared with that of the Pd_{octa}/Pd-S/I NPs. In addition, the cubic Pd NPs also showed better CO removal capability than octahedral Pd NPs (Figure 14b). These results unambiguously corroborate the substantially enhanced CO tolerance of the catalysts with cubic shape due to their {100}-bounded surfaces. Collectively, co-existence of partially sulfurized Pd/Pd-S and {100}-bounded surface in the Pd_{cube}/Pd-S/I NPs can provide them with optimal electronic structures and enhanced CO tolerance, which results in the promotion of their EOR performance.

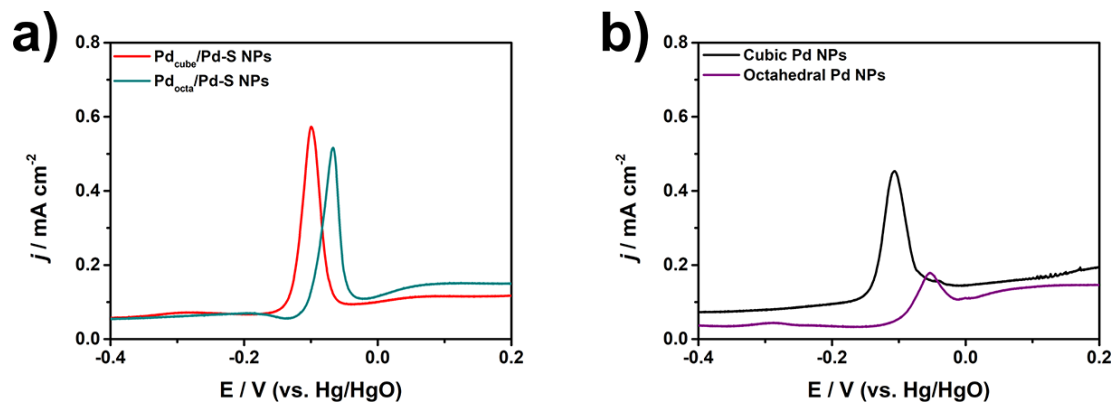


Figure 14. CO stripping measurements on (a) $\text{Pd}_{\text{cube}}/\text{Pd-S/I}$, $\text{Pd}_{\text{octa}}/\text{Pd-S/I}$, (b) cubic Pd, and octahedral Pd NPs.

The catalytic stability of Pd_{cube}/Pd-S/I NPs was investigated by accelerated durability test (ADT) in Ar-saturated 0.5 M KOH + 1 M ethanol solution, and the results were compared with those of cubic Pd NPs and commercial Pd/C catalysts. Figure 15 shows the CVs of the catalysts before and after 300 and 500 EOR cycles. After 300 cycles, the current densities of the Pd_{cube}/Pd-S/I NPs, cubic Pd NPs, and commercial Pd/C in EOR were 1396, 1001, and 600.1 mA mg⁻¹, respectively, which exhibits the higher stability of the Pd_{cube}/Pd-S NPs compared to the other catalysts. After 500 cycles, despite of decrease of the mass activities of the Pd_{cube}/Pd-S/I NPs to 1222 mA mg⁻¹, which are still higher than those of cubic Pd NPs (777.9 mA mg⁻¹) and Pd/C (392.8 mA mg⁻¹) (Figure 15e). Furthermore, the residual current density of the Pd_{cube}/Pd-S/I NPs was about 47.5% of the initial current density, which was higher than those of both cubic Pd NPs (35.3%), and commercial Pd/C (30.2%) (Figure 15f). The TEM image of the Pd_{cube}/Pd-S/I NPs obtained after 500 cycles exhibited well-retained cubic shapes, while some deformation and aggregation were observed in the cubic Pd NPs and commercial Pd/C after stability tests (Figure 16). The enhanced catalytic stability of the Pd_{cube}/Pd-S/I NPs is attributed to surface Pd-S, which can hamper the dissolution and deactivation of Pd during potential operation and thus increase their EOR stability.

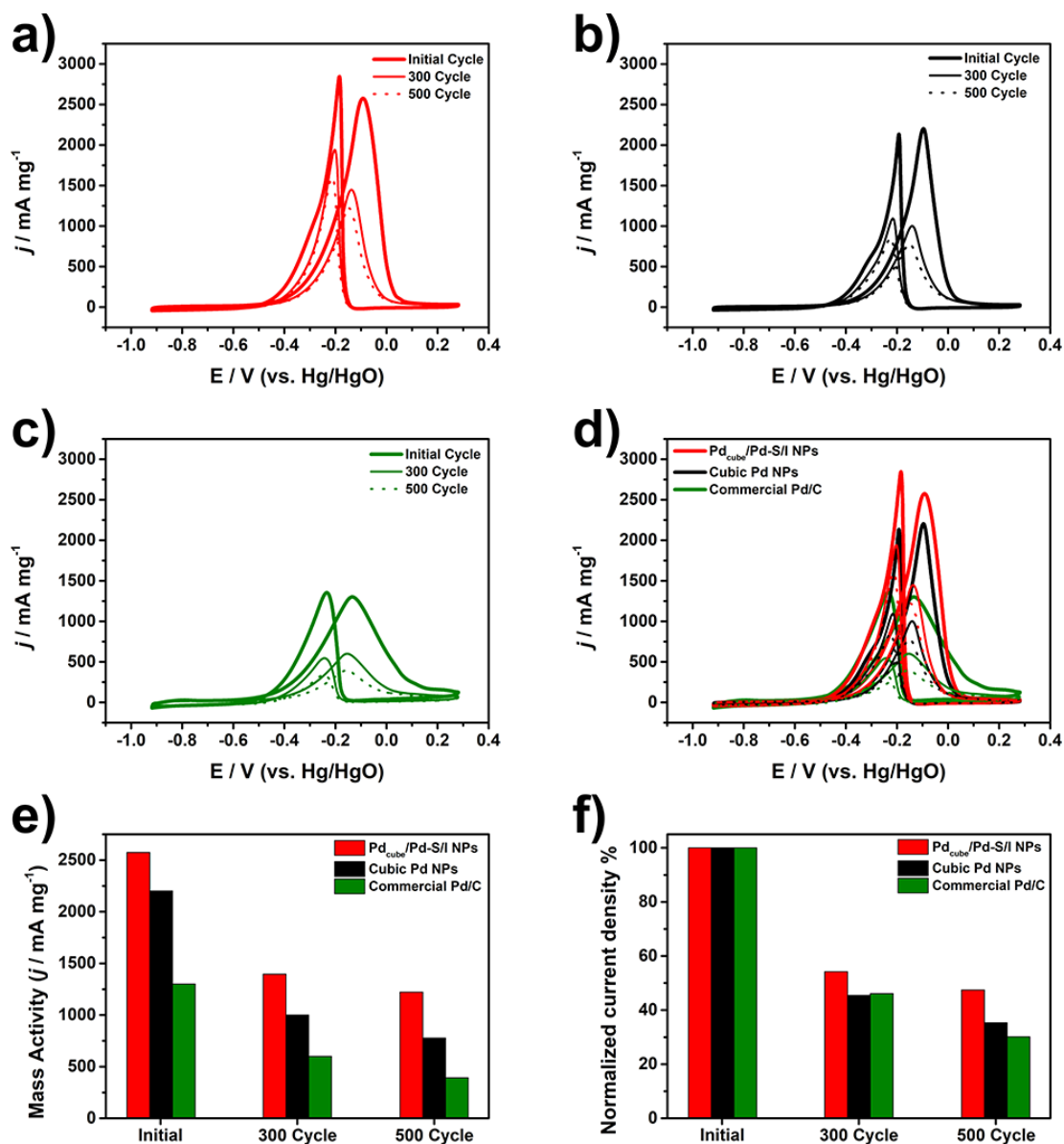


Figure 15. CVs obtained before and after 300 and 500 cycles of (a) Pd_{cube}/Pd-S/I NPs, (b) cubic Pd NPs, (c) commercial Pd/C, and (d) all catalysts. Electrocatalytic stabilities of the catalysts with respect to (e) mass activity and (f) normalized current density.

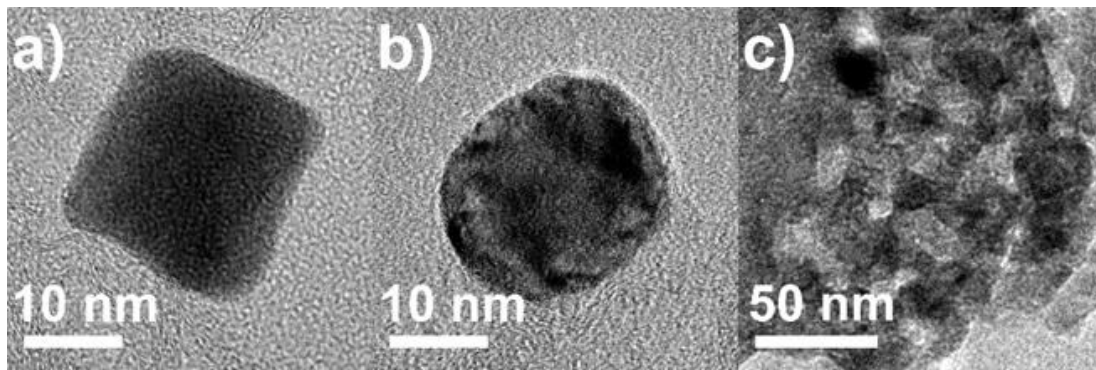


Figure 16. TEM images of (a) Pd_{cube}/Pd-S/I NPs, (b) cubic Pd NPs, and (c) commercial Pd/C after stability tests.

III. Experimental Section

Material and Methods

Chemical and Materials. Sodium tetrachloropalladate(II) (Na_2PdCl_4 , 98%), potassium bromide (KBr, $\geq 99\%$), polyvinylpyrrolidone (PVP, Mw 55,000), Cetyltrimethylammonium chloride solution (CTAC, 25 wt% in H_2O), sodium sulfide nonahydrate ($\text{Na}_2\text{S}\cdot 9\text{H}_2\text{O}$, $\geq 98\%$) and Nafion® perfluorinated resin solution (5 wt%) were obtained from Sigma-Aldrich. Palladium, 20% on activated carbon was obtained from Alfa Aesar. Citric acid (99%) was obtained from Acros Organic, potassium hydroxide (KOH, 95.0%) was obtained from Samchun. L-ascorbic acid (AA, 99.5%) was obtained from Daejung. Other chemicals were reagent grade, and deionized water with a resistivity of greater than $18.3 \text{ M}\Omega\cdot\text{cm}$ was used in the preparation of reaction solutions.

Synthesis of Pd nanocubes. In a typical synthesis of Pd nanocubes, PVP (105 mg), AA (60 mg), and KBr (600 mg) were dissolved in 8.0 mL of deionized (DI) water, and then the solution is heated until $80 \text{ }^\circ\text{C}$ under stirring for 10 min. Subsequently, Na_2PdCl_4 (57 mg) was dissolved in deionized water (3 mL) and then injected into the pre-heated solution. The solution maintained at $80 \text{ }^\circ\text{C}$ for 3 h. The product was washed three times with DI water using a centrifuge, and then re-dispersed in 5 mL of DI water.

Synthesis of Pd nanooctahedra. In a typical synthesis of Pd nanooctahedra, PVP (105 mg), AA (60 mg), and citric acid (60 mg) were dissolved in 8.0 mL of DI water, and then the solution is heated until $100 \text{ }^\circ\text{C}$ under stirring for 10 min. Subsequently, Na_2PdCl_4 (60 mg) was dissolved in DI water (3 mL) and then injected into the pre-heated solution. The solution maintained at $100 \text{ }^\circ\text{C}$ for 3 h. The product was washed three times with DI water using a centrifuge, and then re-dispersed in 5 mL of DI water.

Synthesis of Pd sulfide NPs. In a typical synthesis of Pd sulfide NPs, 1.0 mL of $\text{Na}_2\text{S}\cdot 9\text{H}_2\text{O}$ (5 mM), 1.0 mL of AA (300 mM) were injected in 5.0 mL of CTAC (50 mM), and then the

solution is heated until 100 °C under stirring for 10 min. Subsequently, 1.0 mL of Pd NPs was injected into the pre-heated solution. The solution maintained at 100 °C for 10 min. As soon as end of reaction, the product was washed three times with DI water using a centrifuge. For typical synthesis of Pd/Pd-S/II, Pd@Pd-S, Pd-S, aqueous solution of Na₂S·9H₂O with 10, 30, 100 mM was injected instead of aqueous solution of Na₂S·9H₂O (5 mM), respectively.

Synthesis of Palladium sulfide/C. A suspension of the Pd sulfide NPs in DI water was mixed with 48 mg of Ketjen carbon in DI water under sonication process for 4 h. The product mixture of Pd sulfide/C catalyst was precipitated out by centrifugation at 5,000 rpm. The final catalyst was washed 2 times with DI water and dried for 20 min with Ar purging.

Electrochemical measurements of Pd sulfide NPs. Electrochemical measurements were performed in a three-electrode cell using Bio-logic EC-Lab SP-300. Hg/HgO (1 M NaOH) and Pt wire were used as the reference and counter electrodes, respectively. All electrochemical data was obtained at room temperature. To prepare the working electrode, a 10 μL of the catalyst ink (0.1 mg_{Pd} mL⁻¹ based on ICP-OES, dilution for deionized water) was dropped onto a glassy carbon electrode (GCE, diameter: 5 mm), and then dried at room temperature. After dried then 10 μL of 0.05 wt% Nafion solution was dropped onto dried catalyst, and then dried at room temperature. The dried GCE was washed several times with water and ethanol to remove residual molecules. The dried GCE was further cleaned electrochemically by 50 potential cycles between -0.92 and 0.28 V vs Hg/HgO at a scan rate of 50 mV s⁻¹ in 0.5 M KOH. The electrolyte solutions were purged with N₂ gas for 40 min before performing electrochemical experiments. The CVs of all catalysts were obtained between -0.92 and 0.28 V vs Hg/HgO at a scan rate of 50 mV s⁻¹ in 0.5 M KOH or 0.5 M KOH + 1.0 M ethanol. For CO-stripping experiments, the surface of the catalysts loaded on GCE was saturated with CO by purging CO gas in 0.5 M KOH while holding the working electrode at -0.3 V versus Hg/HgO for 15 min, and then CO dissolved in electrolyte was removed by purging with N₂ gas for 40 min.

Characterizations. TEM and SEM images of the prepared Palladium sulfide NPs were obtained on Jeol JEM-2100F and Jeol JEM-7210F, respectively. Inductively coupled plasma-optical emission spectrometry (ICP-OES) measurement was carried out using a Spectroblue-ICP-OES (Ametek). X-ray diffraction (XRD) measurement were conducted on a Rigaku

D/MAX2500V/PC scanning for 2θ at 20 to 100 degree. X-ray photoelectron spectroscopy (XPS) measurements were conducted on a ThermoFisher K-alpha.

IV. Conclusion

In summary, we have demonstrated an effective wet-chemical synthesis for shape-controlled Pd sulfide NPs with various sulfur distributions. Of different Pd sulfide NPs, Pd_{cube}/Pd-S/I NPs produced by partially sulfurizing the Pd surfaces showed remarkable catalytic performance than their Pd sulfide NP counterparts, cubic Pd NPs, octahedral Pd NPs, and commercial Pd/C catalysts. In addition, enhanced catalytic stability of the Pd_{cube}/Pd-S/I NPs for EOR was observed, which is attributed to their structural and compositional benefits like co-existence of partially sulfurized and {100}-bounded surfaces. This work demonstrates that the EOR activity of the Pd sulfide catalysts is unambiguously dependent on their surface morphology and presence of Pd-S on the surface of the NPs. Given their outstanding catalytic performance in EOR, the Pd sulfide NPs may find broad applications in fuel oxidation, electrochemical reduction, and beyond.

V. Reference

1. Kundu, S.; Patra, A., Nanoscale strategies for light harvesting. *Chem. Rev.* **2016**, *117*, 712-757.
2. Hong, J. W.; Lee, S.-U.; Lee, Y. W.; Han, S. W., Hexoctahedral Au nanocrystals with high-index facets and their optical and surface-enhanced Raman scattering properties. *J. Am. Chem. Soc.* **2012**, *134*, 4565-4568.
3. Liu, L.; Corma, A., Metal catalysts for heterogeneous catalysis: from single atoms to nanoclusters and nanoparticles. *Chem. Rev.* **2018**, *118*, 4981-5079.
4. Hong, J. W.; Wi, D. H.; Lee, S.-U.; Han, S. W., Metal–semiconductor heteronanocrystals with desired configurations for plasmonic photocatalysis. *J. Am. Chem. Soc.* **2016**, *138*, 15766-15773.
5. Shao, M.; Chang, Q.; Dodelet, J.-P.; Chenitz, R., Recent advances in electrocatalysts for oxygen reduction reaction. *Chem. Rev.* **2016**, *116*, 3594-3657.
6. Guo, S.; Zhang, S.; Sun, S., Tuning nanoparticle catalysis for the oxygen reduction reaction. *Angew. Chem. Int. Ed.* **2013**, *52*, 8526-8544.
7. Bian, T.; Zhang, H.; Jiang, Y.; Jin, C.; Wu, J.; Yang, H.; Yang, D., Epitaxial growth of twinned Au–Pt core–shell star-shaped decahedra as highly durable electrocatalysts. *Nano Lett.* **2015**, *15*, 7808-7815.
8. Hong, J. W.; Kim, Y.; Wi, D. H.; Lee, S.; Lee, S. U.; Lee, Y. W.; Choi, S. I.; Han, S. W., Ultrathin Free-Standing Ternary-Alloy Nanosheets. *Angew. Chem. Int. Ed.* **2016**, *55*, 2753-2758.
9. Huang, X.; Zhao, Z.; Fan, J.; Tan, Y.; Zheng, N., Amine-assisted synthesis of concave polyhedral platinum nanocrystals having {411} high-index facets. *J. Am. Chem. Soc.* **2011**, *133*, 4718-4721.
10. Zhang, J.; Ye, J.; Fan, Q.; Jiang, Y.; Zhu, Y.; Li, H.; Cao, Z.; Kuang, Q.; Cheng, J.; Zheng, J.; Xie, Z., Cyclic Penta-Twinned Rhodium Nanobranches as Superior Catalysts for Ethanol Electro-oxidation. *J. Am. Chem. Soc.* **2018**, *140*, 11232-11240.
11. Liu, M.; Zhao, Z.; Duan, X.; Huang, Y., Nanoscale Structure Design for High-Performance Pt-Based ORR Catalysts. *Adv. Mater.* **2019**, *31*, 1802234.
12. Xu, Y.; Zhang, B., Recent advances in porous Pt-based nanostructures: synthesis and electrochemical applications. *Chemical Society Reviews* **2014**, *43*, 2439-2450.

13. Bianchini, C.; Shen, P. K., Palladium-based electrocatalysts for alcohol oxidation in half cells and in direct alcohol fuel cells. *Chem. Rev.* **2009**, *109*, 4183-4206.
14. Chen, A.; Ostrom, C., Palladium-based nanomaterials: synthesis and electrochemical applications. *Chem. Rev.* **2015**, *115*, 11999-12044.
15. Kim, K. S.; Kim, H. C.; Hong, J. W., Controlled Synthesis of Pd Nanocube-Polyaniline Hybrids for Ethanol Oxidation Reaction. *Bull. Korean Chem. Soc.* **2019**, *40*, 78-81.
16. Cerritos, R. C.; Guerra-Balcázar, M.; Ramírez, R. F.; Ledesma-García, J.; Arriaga, L. G., Morphological effect of Pd catalyst on ethanol electro-oxidation reaction. *Materials* **2012**, *5*, 1686-1697.
17. Xia, X.; Choi, S.-I.; Herron, J. A.; Lu, N.; Scaranto, J.; Peng, H.-C.; Wang, J.; Mavrikakis, M.; Kim, M. J.; Xia, Y., Facile Synthesis of Palladium Right Bipyramids and Their Use as Seeds for Overgrowth and as Catalysts for Formic Acid Oxidation. *J. Am. Chem. Soc.* **2013**, *135*, 15706-15709.
18. Jin, M.; Zhang, H.; Xie, Z.; Xia, Y., Palladium nanocrystals enclosed by {100} and {111} facets in controlled proportions and their catalytic activities for formic acid oxidation. *Energy Environ. Sci.* **2012**, *5*, 6352-6357.
19. Ji, L.; Lv, C.; Chen, Z.; Huang, Z.; Zhang, C., Nickel-Based (Photo) Electrocatalysts for Hydrogen Production. *Adv. Mater.* **2018**, *30*, 1705653.
20. Guo, Y.; Park, T.; Yi, J. W.; Henzie, J.; Kim, J.; Wang, Z.; Jiang, B.; Bando, Y.; Sugahara, Y.; Tang, J., Nanoarchitectonics for Transition-Metal-Sulfide-Based Electrocatalysts for Water Splitting. *Adv. Mater.* **2019**, 1807134.
21. Wang, D.-Y.; Gong, M.; Chou, H.-L.; Pan, C.-J.; Chen, H.-A.; Wu, Y.; Lin, M.-C.; Guan, M.; Yang, J.; Chen, C.-W.; Wang, Y.-L.; Hwang, B.-J.; Chen, C.-C.; Dai, H., Highly Active and Stable Hybrid Catalyst of Cobalt-Doped FeS₂ Nanosheets–Carbon Nanotubes for Hydrogen Evolution Reaction. *J. Am. Chem. Soc.* **2015**, *137*, 1587-1592.
22. Huang, Z.-F.; Song, J.; Li, K.; Tahir, M.; Wang, Y.-T.; Pan, L.; Wang, L.; Zhang, X.; Zou, J.-J., Hollow Cobalt-Based Bimetallic Sulfide Polyhedra for Efficient All-pH-Value Electrochemical and Photocatalytic Hydrogen Evolution. *J. Am. Chem. Soc.* **2016**, *138*, 1359-1365.
23. Li, P.; Zeng, H. C., Advanced oxygen evolution catalysis by bimetallic Ni–Fe

- phosphide nanoparticles encapsulated in nitrogen, phosphorus, and sulphur tri-doped porous carbon. *Chem. Commun.* **2017**, *53*, 6025-6028.
24. Du, C.; Li, P.; Yang, F.; Cheng, G.; Chen, S.; Luo, W., Monodisperse palladium sulfide as efficient electrocatalyst for oxygen reduction reaction. *ACS applied materials & interfaces* **2017**, *10*, 753-761.
 25. Feng, Y.; Gago, A.; Timperman, L.; Alonso-Vante, N., Chalcogenide metal centers for oxygen reduction reaction: activity and tolerance. *Electrochimica Acta* **2011**, *56*, 1009-1022.
 26. Ganesan, P.; Prabu, M.; Sanetuntikul, J.; Shanmugam, S., Cobalt sulfide nanoparticles grown on nitrogen and sulfur codoped graphene oxide: an efficient electrocatalyst for oxygen reduction and evolution reactions. *ACS Catal.* **2015**, *5*, 3625-3637.
 27. Yu, L.; Xia, B. Y.; Wang, X.; Lou, X. W., General Formation of M–MoS₃ (M = Co, Ni) Hollow Structures with Enhanced Electrocatalytic Activity for Hydrogen Evolution. *Adv. Mater.* **2016**, *28*, 92-97.
 28. Kim, T.; Park, J.; Jin, H.; Oh, A.; Baik, H.; Joo, S. H.; Lee, K., A facet-controlled Rh₃Pb₂S₂ nanocage as an efficient and robust electrocatalyst toward the hydrogen evolution reaction. *Nanoscale* **2018**, *10*, 9845-9850.
 29. Jiang, J.; Lu, S.; Gao, H.; Zhang, X.; Yu, H.-Q., Ternary FeNiS₂ ultrathin nanosheets as an electrocatalyst for both oxygen evolution and reduction reactions. *Nano Energy* **2016**, *27*, 526-534.
 30. Feng, L.-L.; Yu, G.; Wu, Y.; Li, G.-D.; Li, H.; Sun, Y.; Asefa, T.; Chen, W.; Zou, X., High-Index Faceted Ni₃S₂ Nanosheet Arrays as Highly Active and Ultrastable Electrocatalysts for Water Splitting. *J. Am. Chem. Soc.* **2015**, *137*, 14023-14026.